Supporting Information

3D Printed Electrically-Driven Soft Actuators

Ghazaleh Haghiashtiani [a], Ed Habtour [b, c, d], Sung-Hyun Park [a], Frank Gardea [b], Michael C. McAlpine [a, *]

[a] Department of Mechanical Engineering, University of Minnesota, 111 Church St. SE, Minneapolis, MN 55455, USA
[b] U.S. Army Research Laboratory, Aberdeen Proving Ground, MD 21005, USA
[c] Department of Applied Mechanics, University of Twente, Enschede, NL
[d] The Netherlands Defence Academy, Den Helder, NL

* Corresponding author E-mail address: mcalpine@umn.edu

Material preparation:

In order to prepare the ionic hydrogel ink, individual solutions of lithium chloride (Sigma-Aldrich) and acrylamide monomer (Sigma-Aldrich) in ultrapure water (Millipore) were prepared and combined along with the addition of ethylene glycol (Fisher Chemical). These components were magnetically stirred to obtain a homogeneous solution. At this point, polyacrylamide (Sigma-Aldrich) was added to the solution followed by an overnight magnetic stirring at 60 °C at 1200 rpm. Then, a solution of N, N'-methylenebisacrylamide (Sigma-Aldrich) in ultrapure water and Irgacure 1173 (BASF) was added to the composition and magnetically stirred for an additional 2 hr. The final ionic hydrogel ink was de-foamed using a planetary centrifugal mixer (Thinky ARM-310) at 2200 rpm prior to printing.

The dielectric layer ink was prepared by mixing barium titanate nanoparticles (<100 nm-cubic, Sigma-Aldrich) in the Wacker SEMICOSIL® 912 base using a planetary centrifugal mixer (Thinky ARM-310) at 2000 rpm for 15 mins. Then, the silicone sealant (Loctite® 5039™ Nuva-Sil®) and the UV catalyst (Wacker ELASTOSIL® CAT UV) were added to the

composition and mixed for an additional 10 mins. Due to the relatively fast curing rate of this composition, this ink was printed immediately after preparation.

3D printing of devices:

The 3D printing system comprised a 3-axis robotic dispenser (Fisnar) coupled with a pneumatic fluid dispensing system (Nordson EFD) which allowed for adjustment of the deposition pressure. In addition, a camera unit was incorporated into the 3D printing system to facilitate the adjustment of the z-offset between the syringe tip and the printing substrate (glass slides, typically), as well as visualization of the printing process. A UV system (OmniCure Model S1500) with wavelength range of 320-500 nm was also mounted on the printer platform to enable the post-deposition crosslinking and curing of the ink materials. The synthesized individual material precursors were loaded into separate syringes, attached to the micro-nozzle tips (Nordson EFD), and mounted on the robotic gantry. The device fabrication involved the layer-by-layer deposition of the different material layers. The inner diameter of the dispensing tips, the printing pressure, and speed for each of the materials are summarized in Table S1. In order to enhance the surface uniformity, the passive and dielectric layers were exposed to UV light (~75 mW/cm^2 and ~65 mW/cm^2, respectively) after the complete deposition of individual layers of each of these materials. Prior to deposition of each hydrogel layer, the underlying silicone-based surface was treated with aliquots of 10 wt% benzophenone (Sigma-Aldrich) solution in acetone (~80 µl). After the absorption of benzophenone, the surface of silicone was dried using nitrogen gas and the subsequent hydrogel layer was printed while the entire structure was exposed to UV light (~5 mW/cm^2). In addition, the hydrogel electrodes were printed with 2 mm offset from each of the sides of the underlying layer to prevent the possibility of connection, and thus, shorting of the device. After printing the bottom hydrogel layer and prior to printing the

main dielectric elastomer (DE) layer, the offset between the sides of the hydrogel and the underlying passive layer was filled with the DE ink to facilitate the printing of the main DE layer. Finally, in order to enable the testing of the devices, copper tape was utilized as electric contact leads. The bottom contact lead was inserted during the printing process and prior to the deposition of the bottom hydrogel electrode, and the top contact lead was attached to the top hydrogel layer after printing the device using a small amount of silver paste to secure the attachment.

Mechanical characterization:

Uniaxial tensile tests were performed on 3D printed rectangular specimens for each of the materials with approximate dimensions of $35 \times 5 \times 1$ mm^3 (L × W × H, as printed) using TA Instruments RSA-G2 Extensional DMA Rheometer. The stress-strain curves were constructed for each material using three specimens at a strain rate of 0.5 mm/s.

Rheological characterization:

Rheological characterization of material precursors (uncured state) were performed using a TA Instruments DHR-3 rotational rheometer. The hydrogel precursor was tested using a cone (40 mm, 2º) and plate geometry, while the silicone/$BaTiO_3$ precursor was tested using a parallel plate geometry (25 mm, 500 µm gap) due to its higher viscosity. Viscometry tests were performed from shear rates of 10^{-1} s^{-1} to 10^3 s^{-1}, and oscillatory rheometry tests were performed at a frequency of 1 Hz and oscillatory stresses of 10^{-1} Pa to 10^4 Pa.

Electrical characterization:

Dielectric characterization for silicone/$BaTiO_3$ was conducted using 3D printed circular samples with thicknesses of ~0.9 mm and diameters of 15 mm. An Agilent 16451B dielectric test

fixture (electrode B, diameter=5 mm) coupled with an Agilent 4284A precision LCR meter were utilized to measure the dielectric constants of five samples. The obtained dielectric constant values were used in finite element method (FEM) and analytical models (Table S2).

The resistance of hydrogel electrodes was measured using a Keithley 4200-SCS. The measurements were performed for five 3D printed rectangular specimens with effective dimensions of $10 \times 5 \times 1$ mm^3 (L × W × H). Copper leads were attached to the hydrogel samples using high purity silver paint to reduce contact resistance. Loading/unloading cycles for strains up to 100% were applied to the samples at a rate of 1.5 mm/min using a Deben microtensile tester and the change in resistance was monitored with changing strain. Specifically, a 2-point probe method was used to measure the electrical resistance via applying a current sweep (1-10 μA) and recording the voltage difference at every 10% strain increment.

Device testing:

The setup used for applying high voltage to the DEAs comprised of an SMU (source measurement unit, Keithley 2450, Tektronix), a high voltage (HV) transformer (Q101-5, XP EMCO), and a voltage divider circuit (Fig. S3). The SMU provided the input voltage which was converted to the high voltage level required for actuating the device via the HV transformer. To achieve full-load configuration, the HV transformer was placed in series with a total of 200 MΩ resistors. This configuration produced an output voltage linearly proportional to the input, which improved the accuracy and controllability of the output voltage. In addition, the voltage divider circuit located at the output port of the setup enabled the attenuation and monitoring of the actuation voltage via a digital storage oscilloscope (TDS 2012C, Tektronix) and a digital multimeter (DMM) integrated in the setup ($V_{Read,DMM} \sim \frac{V_{HV}}{695.8}$).

Shear rate calculation during extrusion:

The shear rates experienced by the inks at the deposition nozzle walls during extrusion ($\dot{\gamma}$) can be estimated as follows [1]:

$$\dot{\gamma} = \left(\frac{3n+1}{4n}\right)\frac{8V}{D} \qquad \text{Eq. 1}$$

where, n is the power-law index, which can be obtained by performing a power fit to the experimental data of viscosity (η) versus shear rate ($\dot{\gamma}$) ($\eta = K\,\dot{\gamma}^{n-1}$, with K denoting the flow consistency index). The calculated n values were 0.366 and 0.53 for the DE and ionic hydrogel inks, respectively. In addition, V and D represent the printing speed and the diameter of the deposition nozzle, respectively. Those values are listed in Table S1 for each material system.

Actuation video analysis:

During the DEA testing, the device actuation was recorded visually using a video camera (Nikon D750). The tip displacement of the device in each video was calculated using the "auto-tracker" tool in the Tracker video analysis and modeling software (https://physlets.org/tracker). For this purpose, a template and a key frame was created on the device tip at its initial position. The device tip was marked with a red color during experiments to facilitate this process. During the analysis, the auto-tracker tool scanned throughout the video frames for the best match to the selected template and yielded data on the changes in the position of the device tip over time. This data on the tip displacement versus time was then synced with separate recordings of the time stamps of the applied voltage to obtain the device actuation performance in terms of tip displacement versus applied voltage.

Analytical model:

Materials model:

To account for the material nonlinearities, the stress-strain of each material was modeled using the Neo-Hookean (reduced polynomial) strain energy density [2]:

$$S = C_{10}(I_1 - 3) = \frac{E_o}{6}(I_1 - 3) \quad \text{Eq. 2}$$

where, C_{10} is a constant correlated with the material elastic modulus at the initial stretch, E_o, obtained from the stress-strain experimental data. I_1 represents the first invariant of the right Cauchy-Green deformation tensor. The material response was assumed to be incompressible and isothermal, hence, $\lambda_1\lambda_2\lambda_3 = 1$, where λ_i denote the principle stretches in the 1-2-3 directions and can be expressed as follows for uniaxial deformation:

$$\lambda = \lambda_1 = \frac{l}{l_o}, \lambda_2 = \lambda_3 = \sqrt{\frac{l_o}{l}} \quad \text{Eq. 3}$$

where l_0 and l denote the initial length and the length at the stretched state, respectively. Therefore, I_1 can be defined as:

$$I_1 = \lambda_1^2 + \lambda_2^2 + \lambda_3^2 = \lambda^2 + \frac{2}{\lambda} \quad \text{Eq. 4}$$

Substituting into the strain energy density yields:

$$S = C_{10}(\lambda^2 + 2\lambda^{-1} - 3) \quad \text{Eq. 5}$$

The uniaxial nominal stress can be obtained by differentiating S, with respect to λ, as follows:

$$\sigma = \frac{\partial S}{\partial \lambda} = 2C_{10}(\lambda - \lambda^{-2}) = \frac{E_o}{3}(\lambda - \lambda^{-2}) \quad \text{Eq. 6}$$

Stretch ratio can be related to the engineering strain using $\varepsilon = \lambda - 1$. Substituting this

relationship into Eq. 6, the stress-strain correlation based on the Neo-Hookean material model can be obtained. Using $\sigma = E\,\varepsilon$, one can solve for the change in the elastic modulus as a function of the stretch:

$$E = \frac{E_o}{3}\frac{\lambda - \lambda^{-2}}{\lambda - 1} = 2C_{10}\frac{\lambda - \lambda^{-2}}{\lambda - 1} \quad \text{Eq. 7}$$

The experimental uniaxial tension test data was entered into Abaqus. The C_{10} values for the hydrogel, dielectric layer, and passive layer were then calculated using the Abaqus built-in least squares method to perform the Neo-Hookean material model fit of the experimental stress-strain data.

Kinematic development:

The device was modeled as a cantilever beam with a free length *L* (Fig. S2), which experienced a hyperelastic displacement of its centroid in response to an applied electrical field, and body and external forces. The device bending deflection with respect to the *x* and *z* axes from the base of the beam to point, *s,* and time, *t,* can be described in terms of an axial displacement along x-direction, $u\ (s,t)$, a transverse displacement along z-direction, $w\ (s,t)$, and a rotational angle, θ. Performing a Taylor expansion up to cubic nonlinearities, the device kinematics can be expressed as follows:

$$u = -\frac{1}{2}\int_0^L w'^2 ds \quad \text{Eq. 8}$$

$$\theta \approx w' + \frac{1}{6}w'^3 \quad \text{Eq. 9}$$

$$u' \approx -\frac{1}{2}w'^2 \quad \text{Eq. 10}$$

The axial strain in the dielectric layer is ε_{11}:

$$\varepsilon_{11} = u' - z\,\kappa \qquad \text{Eq. 11}$$

where z is the distance in the vertical direction from the neutral axis, $\bar{z}$. The normalized curvature due to bending is κ, which is defined as [3]:

$$\kappa = \theta' = w'' + \frac{1}{2}w''w'^2 \qquad \text{Eq. 12}$$

The Rayleigh-Ritz method:

The Rayleigh-Ritz method was employed in which an assumed solution was directly substituted into the energy expressions. Mathematically, w can be expressed as a summation of functions from a complete, orthogonal, sufficiently differentiable function set. The advantage of this approach is that each function needs to satisfy only the kinematic boundary conditions. The approximate solutions were assumed in the form:

$$w(x) = q\psi(x) \qquad \text{Eq. 13}$$

where the trial functions, ψ, are known independent comparison functions to denote the mode shapes (curvature due to deflection) of the beam and q represents the generalized coordinates. Substantial numbers of adequate mode shape functions are available in the open literature. The following mode shape was selected for its generalized applicability to beam-like structures with various boundary conditions [4]:

$$\psi(x) = A[\cos\beta x - \cosh\beta x + C(\sin\beta x - \sinh\beta x)] \qquad \text{Eq. 14}$$

where,

$$C = \frac{\sin\beta L - \sinh\beta L + \beta L\bar{M}(\cos\beta L - \cosh\beta L)}{\cos\beta L + \cosh\beta L - \beta L\bar{M}(\sin\beta L - \sinh\beta L)}$$

The modal amplitude constant, A, and the applied external mass ratio, $\bar{M}$ (if applicable), are the byproduct of normalizing the eigenfunction by the distributive mass of the device. The eigenvalue, β, is obtained numerically using MATLAB.

Constitutive modeling:

The constitutive relation for the entire DEA system was modeled similar to piezoelectric devices [5]. Generally, the constitutive relation of a DEA can be expressed as follows [6]:

$$\begin{bmatrix} \boldsymbol{D} \\ \boldsymbol{\epsilon} \end{bmatrix} = \begin{bmatrix} e^{\sigma} & d^{d} \\ d^{c} & s^{\mathbb{E}} \end{bmatrix} \begin{bmatrix} \mathbb{E} \\ \boldsymbol{\sigma} \end{bmatrix} \qquad \text{Eq. 15}$$

where electric displacement, strain, applied electric field and stress vectors are denoted by vectors D, ϵ, $\mathbb{E}$, and σ, respectively. The dielectric layer material constants include the dielectric permittivity at a constant stress σ (e^{σ}), the electric displacement per unit stress at a given electric field (d^{d}), strain per unit electric field at a known stress (d^{c}), and the elastic compliance at a constant electric field $\mathbb{E}$ ($s^{\mathbb{E}}$). It should be noted that d^{c} and d^{d} are numerically identical [6]. Using 1-axis and 2-axis notations to represent the planar directions (x-direction and y-direction, respectively), and the 3-axis to denote the direction along the thickness of the device (z-direction), the axial stress (σ_{11}) in the DE layer – which includes the contribution of the electromechanical strain (Λ) and axial strain (ε) – can be simplified as:

$$\sigma_{11} = E_{11}[\varepsilon_{11} - \Lambda] \qquad \text{Eq. 16}$$

where, E_{11} represents the elastic modulus of the DE layer (obtained from Eq. 7). The electromechanical strain, Λ, of the DE layer with thickness t_d in response to applied voltage V can be defined as [5, 7]:

$$\Lambda = d_{31}\left(\frac{V}{t_d}\right) = \nu\,\frac{\epsilon_o \epsilon_r}{E_{11}}\left(\frac{V}{t_d}\right)^2 \qquad \text{Eq. 17}$$

The Poisson ratio, vacuum permittivity, and relative dielectric permittivity are ν , ϵ_o, and ϵ_r, respectively.

Energy Method Mathematical Formulation:

The potential energy of the DEA with length L and cross section area A can be expressed as follows [7]:

$$P = \frac{1}{2}\int_0^L \int_0^A E(z)(u' - z\,\kappa - \Lambda)^2\, d\alpha ds \qquad \text{Eq. 18}$$

$$P = \frac{1}{2}\int_0^L [\varepsilon_o \quad \kappa]\begin{bmatrix} EA & EI_c \\ EI_c & EI_b \end{bmatrix}\begin{bmatrix} \varepsilon_o \\ \kappa \end{bmatrix} ds - \int_0^L [F_\Lambda \quad M_\Lambda]\begin{bmatrix} \varepsilon_o \\ \kappa \end{bmatrix} ds \qquad \text{Eq. 19}$$

where, A, I_c, and I_b are the cross-section area, coupling inertia, and bending inertia of the device, respectively.

After expansion, the potential energy becomes:

$$P = \frac{1}{2}\int_0^L EAu'^2 ds + \frac{1}{2}\int_0^L EI_b(w''^2 + w''^2 w'^2)ds + \frac{1}{2}\int_0^L EA\Lambda^2\, ds$$
$$+ \int_0^L EI_c u'\left(w'' + \frac{1}{2}w''w'^2\right)ds - \int_0^L F_\Lambda u' ds \qquad \text{Eq. 20}$$
$$- \int_0^L M_\Lambda(w'' + \frac{1}{2}w''w'^2)ds$$

where:

$$EA = \int_0^A E(z)d\alpha\,, EI_c = -\int_0^A E(z)zd\alpha\,, EI_b = \int_0^A E(z)z^2 d\alpha$$

$$F_\Lambda = \int_0^A E(z)\Lambda d\alpha\,, M_\Lambda = -\int_0^A E(z)\Lambda z d\alpha$$

After substituting the assumed solution:

$$P = \frac{1}{2}\left(\int_0^L EA\psi_1'^2 ds\right)q_1^2 + \frac{1}{2}\left(\int_0^L EI_b\psi_2''^2 ds\right)q_2^2 + \frac{1}{2}\left(\int_0^L EI_b\psi_2''^2\psi_2'^2 ds\right)q_2^4$$
$$+ \frac{1}{2}\int_0^L EA\Lambda^2\, ds + \left(\int_0^L EI_c\psi_1'\psi_2'' ds\right)q_1 q_2$$
$$+ \frac{1}{2}\left(\int_0^L EI_c\psi_1'\psi_2''\psi_2'^2 ds\right)q_1 q_2^3 - \left(\int_0^L F_\Lambda\psi_1' ds\right)q_1 \qquad \text{Eq. 21}$$
$$- \left(\int_0^L M_\Lambda\psi_2'' ds\right)q_2 - \frac{1}{2}\left(\int_0^L M_\Lambda\psi_2''\psi_2'^2 ds\right)q_2^3$$

The Euler-Lagrangian method was then applied to the Lagrangian, $L = T - P$, as follows:

$$\frac{\partial}{\partial t}\left(\frac{\partial L}{\partial \dot{q}_i}\right) - \frac{\partial L}{\partial q_i} = Q \qquad \text{Eq. 22}$$

For a static condition and after substituting P into the above formulation, the Euler-Lagrangian equation becomes:

$$k_{le}q_1 + k_{lc}q_2 + k_{nc}q_2^3 = Q_{1,int} + Q_{1,ext} \qquad \text{Eq. 23}$$

$$k_{lc}q_1 + k_{lb}q_2 + 3k_{nc}q_1q_2^2 + k_{nb}q_2^3 - k_{n\Lambda}q_2^2 = Q_{2,int} + Q_{i,ext} \quad \text{Eq. 24}$$

where:

$$k_{le} = EA\int_0^L \psi_1'^2 ds\,, k_{lb} = EI_b\int_0^L \psi_2''^2 ds\,, k_{lc} = EI_c\int_0^L \psi_1'\psi_2'' ds$$

$$k_{n\Lambda} = \frac{3}{2}M_\Lambda\int_0^L \psi_2''\psi_2'^2 ds\,, k_{nb} = 2EI_b\int_0^L \psi_2''^2\psi_2'^2 ds\,, k_{nc} = \frac{1}{2}EI_c\int_0^L \psi_1'\psi_2''\psi_2'^2 ds$$

$$Q_{1,int} = F_\Lambda\int_0^L \psi_1' ds\,, Q_{2,int} = M_\Lambda\int_0^L \psi_2'' ds$$

where k_{le}, k_{lb}, and k_{lc} represent the linear kinematic stiffness coefficient due to extension, bending, and electromechanical coupling, respectively. $k_{n\Lambda}$, k_{nb}, and k_{nc} denote the nonlinear coefficients due to electrical straining, kinematic bending stiffness, and electromechanical coupling, respectively. The generalized internal, Q_{int}, and external, Q_{ext}, forces are due to the electrical potential and external load, respectively. Since k_{lc} and k_{nc} are numerically negligible, the governing equations become:

$$k_{le}q_1 = Q_{1,int} \quad \text{Eq. 25}$$

$$k_{lb}q_2 + k_{nb}q_2^3 - k_{n\Lambda}q_2^2 = Q_{2,int} + Q_{i,ext} \quad \text{Eq. 26}$$

The blocking force is [7]:

$$F_{bl} = \Lambda\, EA \quad \text{Eq. 27}$$

Finite element method (FEM):

A two-dimensional FEM model of the DEA was developed using Abaqus. The material parameters were extracted from the stress-strain test data using the Abaqus built-in strain energy potential function for the hydrogel and passive layers. The Neo-Hookean model appeared to

provide a reasonable fit to the uniaxial stress-strain data with an assumed Poisson ratio for the volumetric response of 0.5. Since Abaqus does not provide constitutive models for hyperelastic dielectric materials, we used the Abaqus isotropic elastic model for piezoelectric materials to model the DE layer, but both d_{31} and E for each electric potential increment were updated based on the interpolations from the stress-strain data for the DE along with values obtained from the analytical model with the compensation factor that closely matched the experimental results. A Poisson ratio of 0.495 was used for the DE material based on the allowable Poisson ratio in the Abaqus code for the dielectric layer [8].

The hydrogel electrodes and passive layer were meshed using 8-node, biquadratic, hybrid plane strain elements with reduced integration (CPE8RH). The dielectric layer was meshed using 8-node, biquadratic, piezoelectric plane strain elements with reduced integration (CPE8RE). Perfect bonding between the layers was assumed; thus, surface-based tie constraints at the interfaces were implemented. The electrical potentials for the layers were coupled to the electrical potentials of the nodes of the supporting structure using linear constraint equations.

The electrical boundary conditions were imposed to the top and the bottom of the dielectric layer, where the bottom electrical voltage was set equal to zero, signifying electrical grounding. The experimental measurements of the voltage input to actuate the device were applied to the top electrical boundary condition. Fixed boundary conditions were applied to the nodes located in the end of the passive layer (7 mm) to emulate the device attachment to the rigid glass substrate during the experiments. Finally, experimental cases with an applied tip mass to the DEA were simulated by adding the effect of gravity and a concentrated force at the tip of the device - with a value corresponding to the applied mass - to the FEM. The remainder of the device parameters used for FEM and analytical model are listed in Table S2.

Supporting Information References:

[1] Q.-H. Nguyen, N.-D. Nguyen, Incompressible non-newtonian fluid flows, Continuum Mechanics-Progress in fundamentals and Engineering applications, InTech, 2012.
[2] D. Nicholson, N. Nelson, B. Lin, A. Farinella, Finite element analysis of hyperelastic components, Appl. Mech. Rev., 51 (1998) 301-320.
[3] A. Nayfeh, P. Pai, Linear and nonlinear structural mechanics, Jon Wiley & Sons, 2004.
[4] E. Habtour, D.P. Cole, S.C. Stanton, R. Sridharan, A. Dasgupta, Damage precursor detection for structures subjected to rotational base vibration, Int J Nonlin Mech, 82 (2016) 49-58.
[5] K. Kadooka, H. Imamura, M. Taya, Experimentally verified model of viscoelastic behavior of multilayer unimorph dielectric elastomer actuators, Smart Mater Struct, 25 (2016) 105028.
[6] J. Sirohi, I. Chopra, Fundamental understanding of piezoelectric strain sensors, J Intel Mat Syst Str, 11 (2000) 246-257.
[7] I. Chopra, J. Sirohi, Smart structures theory, Cambridge University Press, 2013.
[8] Abaqus User Manual, Abaqus Theory Guide. Version 6.14, USA.: Dassault Systemes Simulia Corp, (2014).

Table S1. Printing parameters for different ink materials.

Material	Nozzle Inner Diameter	Pressure	Printing Speed
Passive Layer	330 µm	~1.56 MPa	5 mm/s
DE Layer	410 µm	~ 490 kPa	4 mm/s
Ionic Hydrogel	250 µm	~33 kPa	2 mm/s

Table S2. FEM and analytical model parameters.

Parameter Description	Value
Passive layer-Total length	30 mm
Passive layer-Free length	23 mm
Passive layer-Width	10 mm
Passive layer-Thickness	313 µm
Passive layer-Density	998 kg/m^3
Passive layer-Poisson ratio	0.5
Passive layer-C_{10} (Neo-Hookean model coefficient)	62114.34
Hydrogel electrodes-Total length	26 mm
Hydrogel electrodes-Free length	21 mm
Hydrogel electrodes-Width	6 mm
Hydrogel electrode#1-Thickness	458 µm
Hydrogel electrode#2-Thickness	304 µm
Hydrogel electrodes-Density	1197.5 kg/m^3
Hydrogel electrodes-Poisson Ratio	0.5
Hydrogel electrodes-C_{10} (Neo-Hookean model coefficient)	1721.81
DE layer-Total length	30 mm
DE layer-Free length	23 mm
DE layer-Width	10 mm
DE layer-Thickness	516 µm
DE layer-Density	1127.7 kg/m^3
DE layer-Poisson ratio	0.495
DE layer-C_{10} (Neo-Hookean model coefficient)	14041.79
DE layer-Relative Permittivity	4.16
Device mass	0.626 g

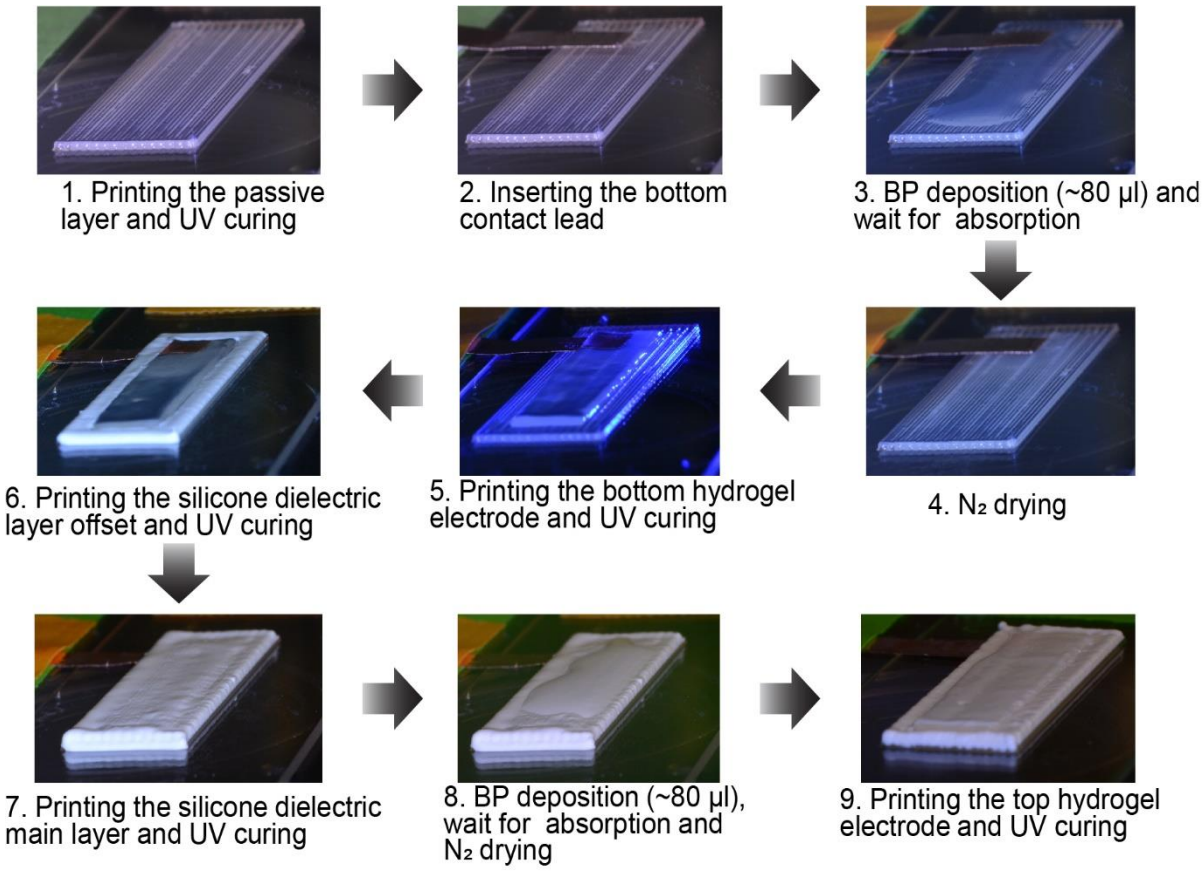

Fig. S1: Step by step fabrication process and 3D printing of the unimorph DEA.

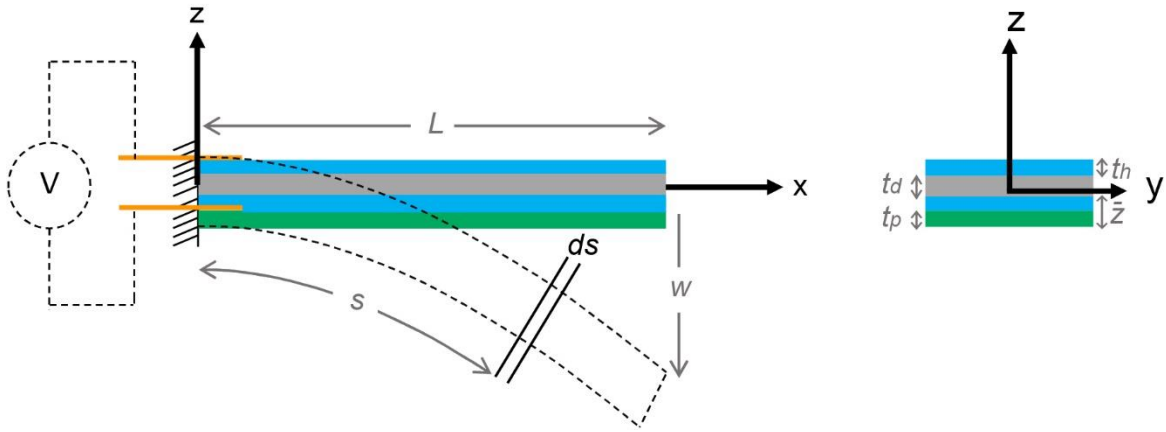

Fig. S2: General schematic of the beam-like device and notations used in the modeling (left), and cross section of the device in which t_p, t_d, and t_h represent the thickness of passive, dielectric, and hydrogel electrode layers, respectively.

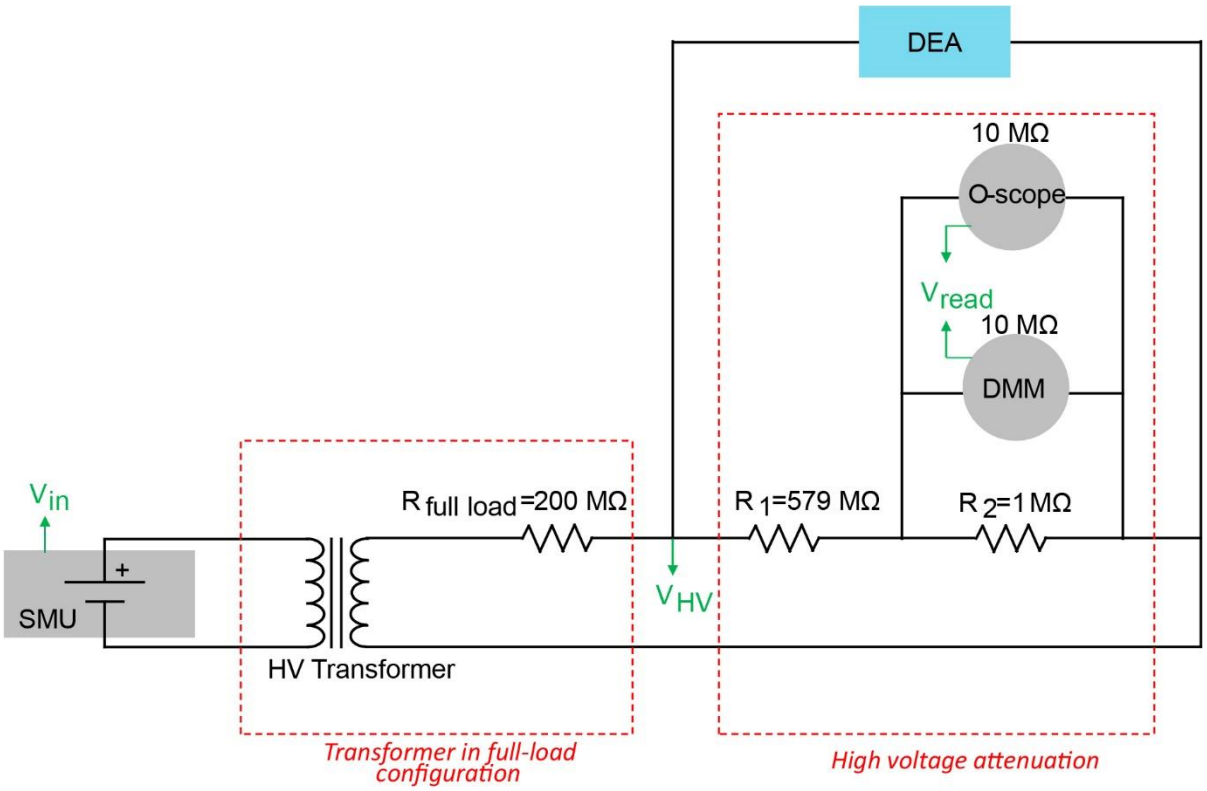

Fig. S3: Circuit setup for high voltage application.

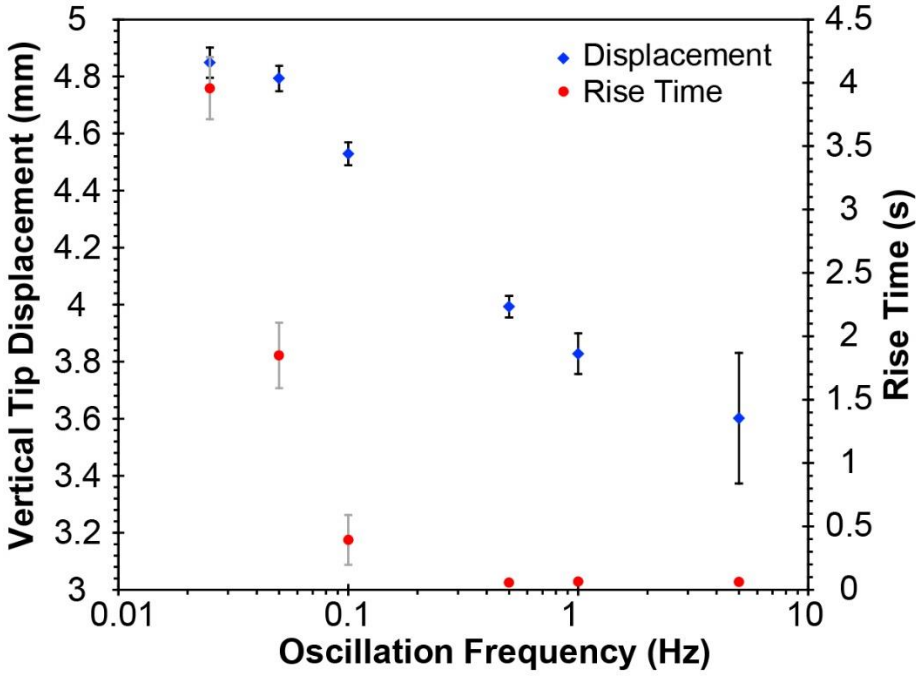

Fig. S4: Effect of changes in the frequency of the square-wave input on DEA displacement and rise time.

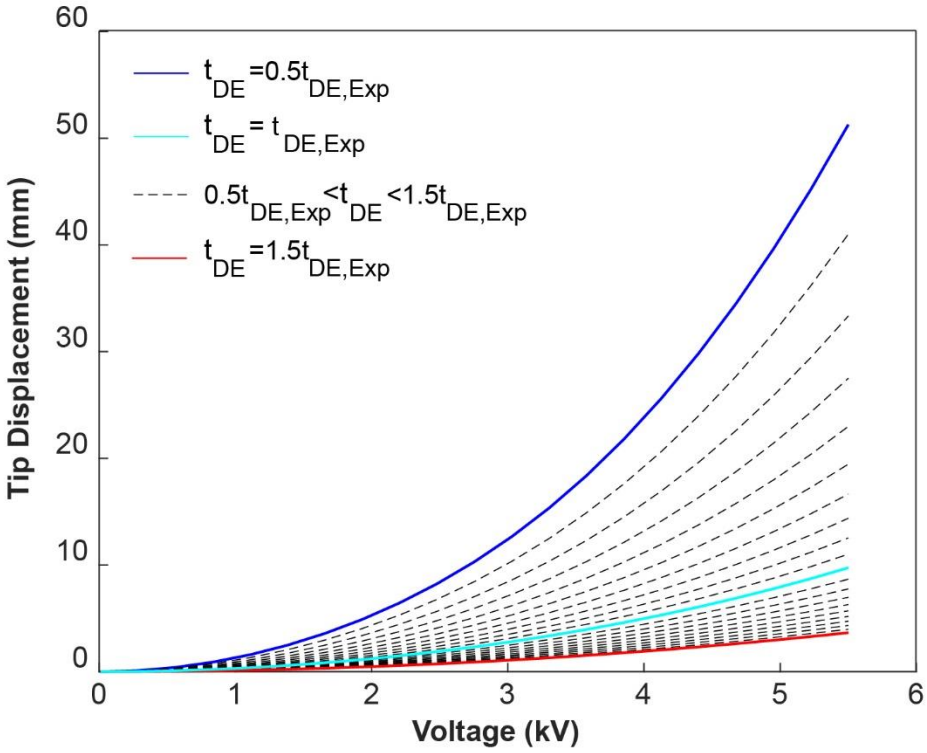

Fig. S5: Effect of changing the DE thickness on device actuation performance.

Movie captions:

Movie 1: Uniform printing of the ionic hydrogel on the silicone-based layer.

Movie 2: Device performance in response to an applied ramp-up voltage.

Movie 3: Device performance in response to an applied cyclic voltage with an amplitude of 4 kV and a frequency of 0.05 Hz.

Movie 4: Device performance in response to an applied tip mass of 0.04 g.